

Prediction of Yield Surface of Single Crystal Copper from Discrete Dislocation Dynamics and Geometric Learning

Wu-Rong Jian^a, Mian Xiao^b, WaiChing Sun^{b,*}, Wei Cai^{a,*}

^a*Department of Mechanical Engineering, Stanford University, Stanford CA, 94305, USA*

^b*Department of Civil Engineering and Engineering Mechanics, Columbia University, 614 SW Mudd, 4709, New York, NY 10027, USA*

Abstract

A yield surface of a material is a set of critical stress conditions beyond which macroscopic plastic deformation begins. For crystalline solids, plastic deformation occurs by the motion of dislocations, which can be captured by discrete dislocation dynamics (DDD) simulations. In this paper, we predict the yield surfaces and strain-hardening behaviors using DDD simulations and a geometric manifold learning approach. The yield surfaces in the three-dimensional space of plane stress are constructed for single-crystal copper subjected to uniaxial loading along the [100] and [110] directions, respectively. With increasing plastic deformation under [100] loading, the yield surface expands nearly uniformly in all directions, corresponding to isotropic hardening. In contrast, under [110] loading, latent hardening is observed, where the yield surface remains nearly unchanged in the orientations in the vicinity of the loading direction itself, but expands in other directions, resulting in an asymmetric shape. This difference in hardening behaviors is attributed to the different dislocation multiplication behaviors on various slip systems under the two loading conditions.

*Corresponding author

Email addresses: wsun@columbia.edu (WaiChing Sun), caiwei@stanford.edu (Wei Cai)

1. Introduction

Understanding crystal plasticity in terms of fundamental physics has been a long-standing goal in computational materials science. Since the proposal of crystal dislocations (Taylor, 1934; Polanyi, 1934; Orowan, 1934) and their observation by transmission electron microscopy (Hirsch et al., 1956), it has been well-established that the plastic deformation behaviors of crystalline materials are controlled by the motion of dislocations (Hirth and Lothe, 1982). The discrete dislocation dynamics (DDD) simulation method (Amodeo and Ghoniem, 1990; Devincre and Kubin, 1997; Arsenlis et al., 2007) has been developed to establish the connection between the microscopic motion of individual dislocations and the macroscopic stress-strain behavior of the single-crystalline material. A fundamental concept in describing the plastic deformation behavior of materials is the yield surface (Meyers and Chawla, 2008). When the local stress at a material point is within the yield surface, the deformation is purely elastic. By contrast, when the local stress reaches the yield surface, plastic deformation begins. Furthermore, the strain-hardening behavior corresponds to the change of the yield surface with increasing plastic strain. For example, isotropic hardening corresponds to the uniform expansion of the yield surface in all directions, while kinematic hardening corresponds to the translation of the yield surface in the stress space without changing its size and shape (Hill, 1998). The Bauschinger effect (Bauschinger, 1886), in which the plastic deformation causes yield stress in the reverse loading direction to become lower, is a manifestation of non-isotropic hardening behavior. Given the central role of yield surface in plasticity and solid mechanics, it would be a natural goal to predict the yield surface of single crystals by DDD simulations. However, to our best knowledge, there have not been predictions of yield surface from DDD simulations to date.

There have been several challenges that have prevented DDD predictions of yield sur-

faces for single crystals. First, DDD simulations have been computationally very expensive. On the one hand, in order to predict the plastic deformation behavior of a crystal, the motion of dislocations in a large enough simulation cell needs to be followed for a long enough time to accumulate a significant level of plastic strain. On the other hand, interactions between nearby dislocations require a very small time step to ensure numerical stability. Second, to construct the yield surface for a given computational sample (i.e. a dislocation configuration) by brute-force DDD simulations would require a very large number of DDD simulations, each with a different loading (stress) orientation. Given that the stress conditions span a six-dimensional (6D) parameter space, the total number of DDD simulations is overwhelming if a uniform sampling is used. Dealing with crystal plasticity, we cannot reduce the stress space to the three-dimensional (3D) space of the principal stresses, because the orientation of the stress with respect to the slip systems of the crystal matters for the forces on dislocations and the yielding behavior. Third, we need a framework to express the yield surface that is flexible enough to fit to the data from DDD predictions, as well as providing mathematically well-behaved interpolation in-between. Ideally, the framework should also inform us where more sampling is needed in the stress space where additional DDD simulations can be performed to provide the most valuable information about the yield surface.

In this work, we construct the yield surfaces of single-crystal Cu from DDD simulations with the following approaches to address the above challenges. First, recent progress on subcycling integrator ([Sills et al., 2016](#)) and GPU implementation ([Bertin et al., 2019](#)) has made DDD simulations much more efficient than before. For single crystal Cu, plastic strain on the order of 1% strain can be reached using a single GPU over the time period of a week, although the strain rate still needs to be kept high (e.g. 10^3 s^{-1}) in these simulations. In this work, we will keep our effective strain rate to be about 10^3 s^{-1} . Hence, our predicted yield surface is not the same as the one typically might have in mind, i.e. for

quasi-static loading conditions. Our work represents a first attempt at this problem, and the strain rate effect on the yield surface will be examined in the future. In addition, we show that if we just need to determine the yield point for a given loading direction, the DDD simulation can be much shorter than what is needed for determining the strain hardening rate. Second, in order to reduce the total number of DDD simulations, here we will limit our scope to the plane-stress condition, where only three stress components are non-zero. This means that we will construct a 3D “cross-section” of the full yield surface which lives in the 6D space. The yield surface in the 3D plane-stress conditions is also much easier to visualize, and we show that quite interesting insights can be gained by examining how it evolves while the crystal is plastically deformed along different loading directions. Third, we use the geometric prior method ([Xiao and Sun, 2022](#)) to construct the yield surface from the DDD simulation data, where patches each having a local coordinate system provide smooth local descriptions of the yield surface, respectively. Then, the patches overlap consistently and offer a general description of any surface. The geometric prior framework can provide ways to evaluate local features on the yield surface, e.g. local curvature, which can be used to decide where more data should be collected from additional DDD simulations. Prior to the geometric prior method, the non-uniform rational B-spline (NURBS) method ([Coombs et al., 2016](#); [Coombs and Motlagh, 2017, 2018](#)) and the level-set function ([Vlassis and Sun, 2021, 2022](#)) had also been developed to construct yield surfaces. Compared to the geometric prior method that employs various trainable neural networks in different patches, both NURBS and level-set approaches use a single learned function to represent the yield surface, and the resultant models are difficult to update when new data are supplemented from DDD simulations. Hence, they are not suitable for an active learning environment where the learned yield surface must be easily updated (i.e., without re-training the entire model from scratch) whenever new data is presented. While we demonstrate yield surface in the 3D plane-stress space, our geometric prior framework to

construct yield surface is equally applicable to the full 6D stress space.

The rest of this paper is organized as follows. First, the DDD simulation setup and the procedure of yield stress data extraction from DDD simulation are described in Section 2.1, followed by the details of our yield surface construction framework using geometric prior in Section 2.2. We present the 3D yield surfaces of various dislocation configurations of single-crystal Cu upon plane stress loading in Section 3.1 and the 2D yield loci for uniaxial loading in Section 3.2. The results show that the yield surface evolves in different modes during the strain hardening of single-crystal Cu along [100] (isotropic hardening) and [110] (latent hardening), respectively. Section 4.1 gives an explanation of this observation based on the different dislocation multiplication behaviors on various slip systems for these two loading orientations. The outlooks for DDD simulations and the geometric prior method for the yield surface construction of single crystals are provided in Section 4.2 and Section 4.3, respectively. The conclusions are given in Section 5.

2. Methodology

2.1. Data collection from DDD

The DDD simulations are conducted using the open-source ParaDiS program ([Arsenlis et al., 2007](#); [ParaDiS, 2023](#)), which utilizes the recently developed sub-cycling time integration scheme ([Sills et al., 2016](#)) and its Graphics Processing Units (GPU) implementation ([Bertin et al., 2019](#)). The material parameters in our DDD simulations correspond to single crystal copper, e.g., Burgers vector magnitude $b = 0.255$ nm, Poissons ratio $\nu = 0.324$, and shear modulus $\mu = 54.6$ GPa. During all DDD simulations, a linear mobility law with drag coefficient $B = 1.56 \times 10^{-5}$ Pa · s is applied to glissile dislocations. Cross-slip is not allowed, and dislocation junctions are only allowed to move along their line directions using zipping or unzipping mode. All the DDD simulation parameters are also summarized

in Table B.1. Due to the large amount of simulations necessary to obtain a yield surface in the general 6D stress space, here we limited our attention to plane stress conditions, where only σ_{xx} , σ_{yy} , σ_{xy} may be non-zero.

The dimensions for the simulation model are $\sim 15 \mu\text{m} \times 15 \mu\text{m} \times 15 \mu\text{m}$. To build the initial dislocation configuration for the subsequent loading simulations, straight dislocation lines on the $\frac{1}{2}\langle 110 \rangle\{111\}$ slip systems are introduced randomly to the simulation box, where periodic boundary conditions (PBCs) are applied along all three directions. The dislocation configuration is then relaxed, resulting in a dislocation density of $\rho_0 \approx 1.2 \times 10^{12} \text{ m}^{-2}$. The relaxed configuration, shown in Figure 1 and also used in our previous works (Akhondzadeh et al., 2020, 2021), is labelled config-0, and considered as the reference configuration in this work.

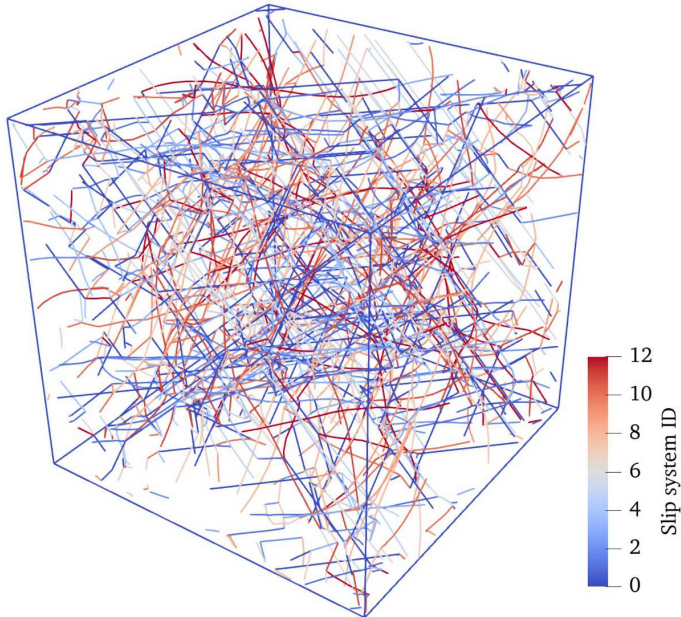


Figure 1: The initial dislocation configuration (config-0) with a dislocation density of $\rho_0 \approx 1.2 \times 10^{12} \text{ m}^{-2}$ before loading in DDD simulation.

To construct the yield surface of a given (relaxed) dislocation configuration, we per-

form a set of DDD simulations, each at a different stress orientation, under a constant stress rate. We choose a coordinate system whose axes are aligned with the cubic axes of the single crystal, i.e. the x , y , z -axes are along the [100], [010], [001] directions, respectively. For simplicity, we focus on the plane stress condition (in the x - y plane, i.e. the (001) crystallographic plane) where the non-zero stress components are limited to σ_{xx} , σ_{yy} and σ_{xy} . In this case, the magnitude and orientation of the stress tensor σ can be visualized by considering a 3D vector $\vec{\sigma} = (\sigma_{xx}, \sigma_{yy}, \sqrt{2}\sigma_{xy})$. This is because the magnitude of stress as given by the Frobenius norm

$$\sigma = \|\sigma\| = \sqrt{\sigma_{xx}^2 + \sigma_{yy}^2 + 2\sigma_{xy}^2}, \quad (1)$$

is the same as the length of the vector $\vec{\sigma}$. Therefore, for every plane stress state with non-zero magnitude, we can define a unit vector, $\hat{\sigma} = \vec{\sigma}/\sigma$, which specifies the stress orientation. Hence all stress orientations in plane stress correspond to a unit sphere in the 3D space of $(\sigma_{xx}, \sigma_{yy}, \sqrt{2}\sigma_{xy})$. To construct the yield surface under plane stress, we thus need to sample the stress orientation $\hat{\sigma}$ from this unit sphere, and for each chosen $\hat{\sigma}$ increase the stress magnitude $\|\sigma\|$ linearly with time until yielding is detected.

Our initial sampling of the plane stress space corresponds to 92 points nearly uniformly distributed on the unit sphere, which are the vertices of the polyhedron shown in [Figure 2](#). The coordinates of the sampling points are obtained using the icosphere module in Python ([Dahl, 2023](#)). The uniaxial loading conditions along different directions in the x - y plane are shown as the red circle on the unit sphere in the 3D space of plane stress.

For each stress orientation shown in [Figure 2](#), we performed a DDD simulation in which the stress orientation remains fixed and the stress magnitude increases at a constant rate $\dot{\sigma} = 10^{13} \text{ Pa} \cdot \text{s}^{-1}$. The magnitude of the stress rate is chosen here so that the stress-strain response of the single crystal upon uniaxial loading condition matches those at a strain rate of 10^3 s^{-1} , which is a common strain rate used in DDD simulations of single

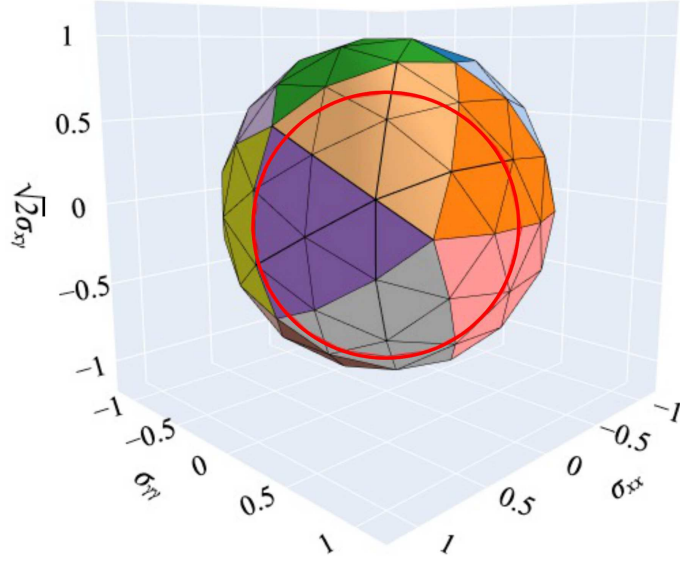


Figure 2: A total of 92 points distributed nearly uniformly on the unit sphere are shown as vertices of a polyhedron generated by the icosphere module in Python (Dahl, 2023). The red circle corresponds to uniaxial tensile loading along different directions in the x - y plane.

crystal Cu (Sills et al., 2018; Bertin et al., 2019; Akhondzadeh et al., 2020, 2021). For example, Figure A.1 shows that for uniaxial tensile loading along [100] crystal orientation, the stress-strain curves for constant stress rate of 10^{13} Pa \cdot s $^{-1}$ and constant strain rate of 10 3 s $^{-1}$ are consistent with each other up to the yielding point.

To plot the stress-strain curves for a general plane stress loading, we define the strain (in the horizontal axis) as the dot product between the stress and strain tensors,

$$\varepsilon^{\text{pl}} = \hat{\sigma}_{xx}\varepsilon_{xx}^{\text{pl}} + \hat{\sigma}_{yy}\varepsilon_{yy}^{\text{pl}} + 2\hat{\sigma}_{xy}\varepsilon_{xy}^{\text{pl}} \quad (2)$$

where $\hat{\sigma}_{xx} = \sigma_{xx}/\|\sigma\|$, $\hat{\sigma}_{yy} = \sigma_{yy}/\|\sigma\|$, $\hat{\sigma}_{xy} = \sigma_{xy}/\|\sigma\|$. $\varepsilon_{xx}^{\text{pl}}$, $\varepsilon_{yy}^{\text{pl}}$ and $\varepsilon_{xy}^{\text{pl}}$ are the plastic strain components. This definition reduces to the normal plastic strain along the loading direction for the case of uniaxial loading. In this work, the yield point of plane stress loading is determined by $\varepsilon^{\text{pl}} = 0.022\%$. This yield criterion is the same as using the strain

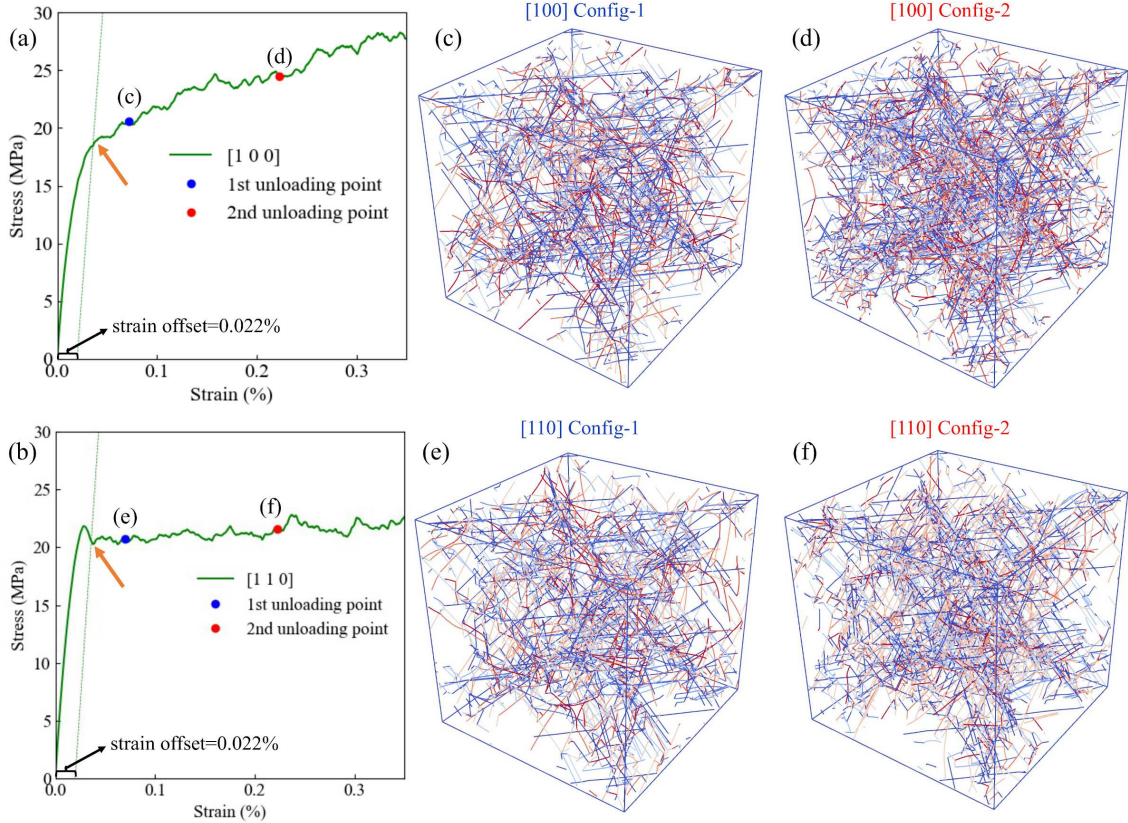


Figure 3: (a-b) The stress-strain curves for the uniaxial tensile loading at strain rate 10^3 s^{-1} along [100] and [110] directions, respectively. The blue and red dots on the curves represent the unloading points at the strains of 0.07% and 0.22%, where dislocation configurations are extracted and relaxed, respectively. The yield point is determined as the intersection of the curve with the elastic curve offset of 0.022%, as denoted by the orange arrows. (c-d) show the corresponding relaxed dislocation configurations from the [100] loading, respectively. (e-f) show the corresponding relaxed dislocation configurations corresponding from the [110] loading curve, respectively.

offset in the case of uniaxial loading, when applied to the stress-strain curve in which the strain is the total strain, as shown in Figure 3(a) and (b). The choice of 0.022% offset strain is similar to those used in previous experimental work (Franciosi et al., 1980).

To investigate how the yield surface evolves by strain hardening, we also computed

the yield points along the stress orientations defined in [Figure 2](#) for four more dislocation configurations. These configurations are obtained from DDD simulations starting from config-0 as initial condition, and subjected to uniaxial tensile loading conditions with strain rate 10^3 s^{-1} , along the [100] and [110] directions, respectively. For each loading orientation, two configurations are extracted at the strains of 0.07% and 0.22%, and unloaded to zero stress and relaxed, leading to config-1 and config-2, respectively. These four dislocation configurations are plotted in [Figure 3\(c\), \(d\), \(e\) and \(f\)](#), respectively. From the normal stress-strain curves in [Figure 3\(a\) and \(b\)](#), it can be seen that the [100] loading orientation has a higher strain hardening rate than the [110] loading orientation. This is because for [100] loading, all 4 slip planes and 8 out of 12 slip systems are active, and their intersections lead to a high strain hardening rate. In contrast, for [110] loading, only 2 slip planes and 4 slip systems are active. However, the stress-strain curves in [Figure 3\(a\) and \(b\)](#) only reveal how the yield point changes along the same stress orientation as the direction of applied loading. In this work, our goal is to determine how the yield surface changes with plastic deformation, i.e. how the yield point changes in all stress orientations most of which do not coincide with the direction of applied loading.

2.2. Construction of yield surface with geometric prior method

We use the method of geometric prior ([Xiao and Sun, 2022](#)) to construct the yield surface (\mathcal{S}) under plane stress as a manifold atlas in \mathbb{R}^3 , based on the yield point data predicted by DDD simulations along a discrete set of stress orientations (\mathcal{X}). The method of geometric prior also allows us to iteratively improve the yield surface representation, by providing suggestions on stress orientations where new DDD simulations can be performed to improve the data density in regions most needed.

We characterize the mathematical representation of the yield surface as a manifold atlas rather than the traditional implicit yield function representation ([Hill, 1998](#)). One can

draw an analogy between a manifold atlas and a piece-wise function: (1) the domain of the piece-wise function is divided into multiple pieces; similarly, the manifold atlas also partitions the surface into multiple patches. (2) On each piece of the domain, the piece-wise function is defined continuously, either explicitly or implicitly; correspondingly, each patch of the manifold atlas is associated with a coordinate chart, a neural network-trained nonlinear mapping that enables us to provide local coordinates of the patch within the yielding manifold. An example of this representation is shown in [Figure 4](#).

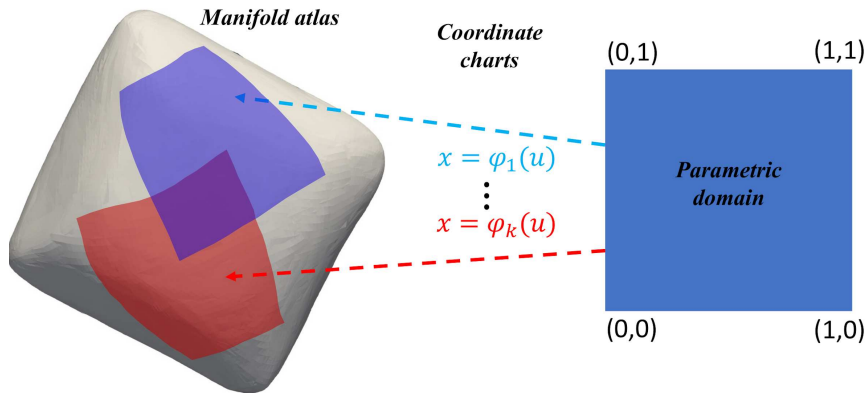


Figure 4: Sketch of the geometric prior manifold representation. The Riemann surface is divided into multiple pieces (patches), and each patch is associated with a coordinate chart as a mapping from a regular parametric domain.

After constructing the initial manifold atlas based on DDD simulation data of 92 stress orientations, we can compute local geometric information, e.g. Gaussian curvature, everywhere on the yield surface. We then identify regions where local refinement is desirable. These are regions where the yield surface intersects a bounding sphere of a chosen radius and centered at points of local maxima of Gaussian curvature. A point cloud is generated in each of these refinement regions using Poisson disk sampling. Additional DDD simulations are then performed to predict yield points at stress orientations corresponding to these new sampling points. The data is combined with the previously obtained DDD data

to obtain a refined manifold atlas representing the updated yield surface. The process can be iterated to sequentially refine the yield surface representation, as illustrated in [Figure 5](#).

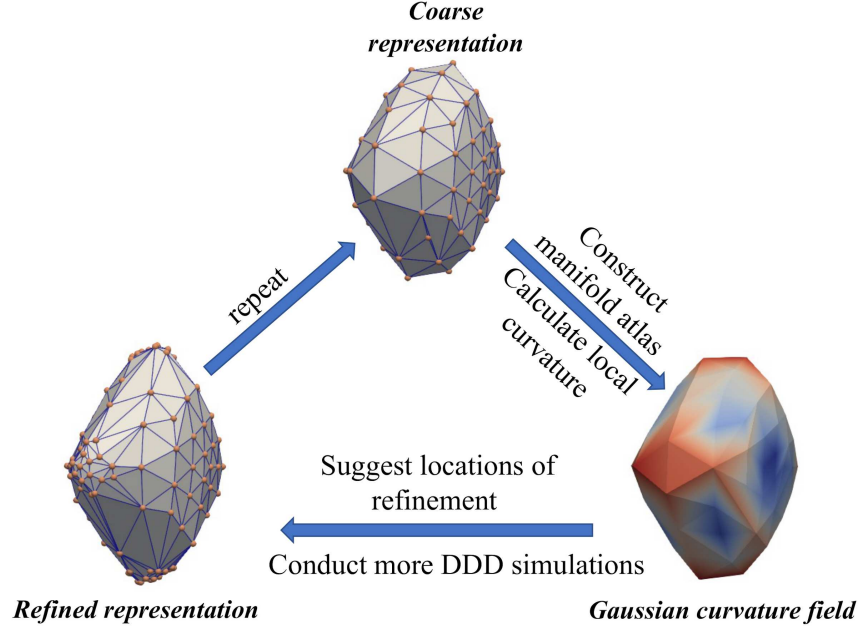


Figure 5: Major steps in the reconstruction of a yield surface.

2.2.1. Geometric prior method for yield surface construction

Here we provide some specifics of the geometric prior method that is applied to constructing the yield surface \mathcal{S} under plane stress as a manifold atlas in \mathbb{R}^3 ; for more details please refer to ([Xiao and Sun, 2022](#)). To generate the patch discretization of \mathcal{S} , we prescribe a set of anchor points \vec{x}_p on \mathcal{S} . Then, a surface patch \mathcal{S}_p is defined by the intersection of the neighborhood ball at \vec{x}_p and \mathcal{S} : $\mathcal{S}_p = \mathcal{S} \cap \mathcal{B}_p$, $\mathcal{B}_p = \{\vec{x} \in \mathbb{R}^3 \mid \|\vec{x} - \vec{x}_p\| < \epsilon\}$, where ϵ is the radius of the neighborhood ball and $\|\cdot\|$ is the L2-norm. We then define the parametrization of the local coordinate charts as $\phi_p(\vec{v}) : V \rightarrow \mathbb{R}^3$, where $V = (0, 1) \times (0, 1)$.

Subsequently, there are two major learning tasks: (1) fit the local coordinate charts $\phi_p(\vec{v})$; (2) ensure the consistency between patches. The first task is achieved by approx-

imating each coordinate chart with a multi-layer-perceptron (MLP) function (Murtagh, 1991) and optimizing the learnable parameters with the Sinkhorn regularized distance (Cuturi, 2013):

$$\mathcal{L}_p = \min_{P_{ij}} \sum_{i,j \leq N_p} P_{ij} \|\phi(\vec{v}_j; \mathbf{W}_p) - \vec{x}_j\|^2 + \chi^{-1} \sum_{i,j \leq N_p} P_{ij} \log P_{ij} \quad (3)$$

where \mathcal{L}_p is the training loss function and \mathbf{W}_p is the set of neural network parameters for the p th coordinate chart, such that $\phi_p(\vec{v}) \approx \phi(\vec{v}; \mathbf{W}_p)$. N_p is the number of sampling points used to calculate the Sinkhorn distance, which is less than or equal to the total available points within the same coordinate chart. $\vec{v}_j \in V$ indicates the input samples following the Poisson disk distribution for the reconstructed set. P_{ij} is an $n \times n$ bi-stochastic matrix. χ is a regularization parameter such that \mathcal{L}_p approximates the optimal transport distance (Rubner et al., 1997) as $\chi \rightarrow \infty$.

The second task is performed in two steps: we first find the optimal indices permutation policy of each patch p via the following objective derived from (3):

$$\min_{\mathbf{W}_p} \inf_{\pi_p} \sum_{i \leq N_p} \|\phi(\vec{v}_i; \mathbf{W}_p) - x_{\pi_p(i)}\|^2 \quad (4)$$

where π_p is a permutation policy, assigning indices of points in \mathcal{X}_p to indices of parametric positions in V_p . We then minimize the divergence between embedding functions ϕ_p, ϕ_q for all pairs of overlapping patches:

$$\min_{\mathbf{W}_p, \mathbf{W}_q} \inf_{\pi_p, \pi_q} \sum_{i \in T_{pq}} \|\phi(\vec{v}_i; \mathbf{W}_p) - \phi(\vec{v}_{\pi_q^{-1}(\pi_p(i))}; \mathbf{W}_q)\|^2 \quad (5)$$

where $T_{pq} = \{i \mid \vec{x}_{\pi_p(i)} \in \mathcal{X}_p \cap \mathcal{X}_q\}$ indicates the set of indices of parametric points in chart p included within the intersection of chart p and q .

2.2.2. Local refinement of yield surface representation

The initial (nearly uniform) sampling of the plane stress conditions provides an overall representation of the yield surface that may be too coarse. Because of the substantial

computational cost of DDD simulations, it is preferable to locally refine the yield surface representation in regions with sharp edges or corners than a uniform refinement. Similar to mesh refinement (Berger and Oliger, 1984) in numerical simulations, the point cloud (for which DDD predictions are collected) should be densified at the locations where it is likely to provide the most information gain. In geometry reconstruction, we believe curvature is a reasonable choice of quantitative criterion for such purpose (Tang and Feng, 2018).

There are multiple curvature measures in the application of geometric learning. In order to efficiently establish a criterion with inequality, we adopted one of the scalar curvature measures: Gaussian curvature (Kreyszig, 2013), denoted as \mathcal{K} (for mathematical formulation of Gaussian curvature, please refer to (Xiao and Sun, 2022)). Gaussian curvature can serve as a smoothness measure for digital images and geometric objects (Tang et al., 2023), where a large Gaussian curvature usually indicates a relatively abrupt change in the geometric shape (e.g. non-smoothness). Here we selected regions for enrichment as locations where $\mathcal{K} > 0.07 \text{ MPa}^{-2}$. As Figure 5 shows, such locations group together around the “corners” of the yield surface. For each of the corners, we then defined a bounding sphere $\mathcal{B}^{(e)}$ with minimum radius $R^{(e)}$ that includes all the selected data points (whose $\mathcal{K} > 0.07 \text{ MPa}^{-2}$), where the superscript e labels the enrichment regions (corners).

To refine the yield surface inside the bounding sphere $\mathcal{B}^{(e)}$, we first projected the bounding sphere onto the unit sphere \tilde{S}^2 centered at the origin. The projection is defined as $\mathcal{P}_{\tilde{S}^2}(\mathcal{B}^{(e)})$. We used Poisson disk sampling (Bowers et al., 2010; Williams, 2022) to generate a random but relatively uniform distribution of points over the entire unit sphere \tilde{S}^2 and extracted sampling points that lie within $\mathcal{P}_{\tilde{S}^2}(\mathcal{B}^{(e)})$. Each one of these sampling points on the unit sphere represents a stress orientation $\hat{\sigma}$ for which a DDD simulation is performed under constant stress rate loading to determine the yield point.

To determine how many sampling points are needed in the refined regions, we monitor the convergence of the local Gaussian curvature predicted by the geometric prior at a given

stress orientation, $\hat{\sigma} = \left(-\frac{\sqrt{2}}{2}, -\frac{\sqrt{2}}{2}, 0\right)$. [Figure 6](#) plots the predicted Gaussian curvature at this point when 33, 67 and 97 additional data points are combined with the initial 92 data points to construct the yield surface manifold. We observe a gradual increase of the predicted local Gaussian curvature and an indication of convergence. Due to the limitations of computational resources, we limit the total number of sampling points on the unit sphere to 189, with each sampling point corresponding to a DDD simulation at a different stress orientation.

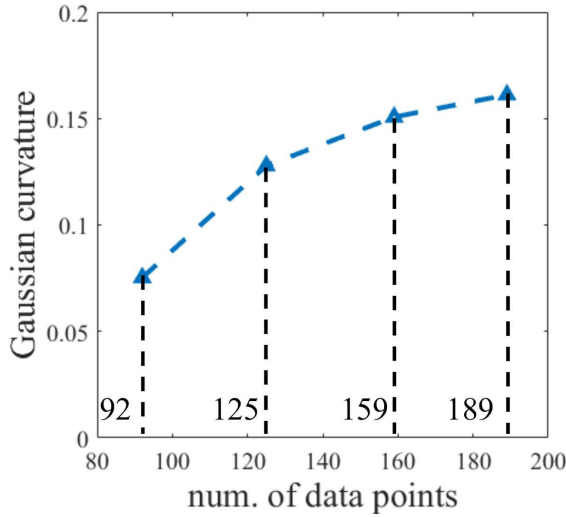


Figure 6: Gaussian curvature of the learned yield surface manifold for config-0 at the stress orientation $\hat{\sigma} = \left(-\frac{\sqrt{2}}{2}, -\frac{\sqrt{2}}{2}, 0\right)$ as a function of the total number of stress orientations used to construct the yield surface manifold.

The geometric learning process is then applied to the enriched dataset to produce a relatively more accurate representation of the DDD yield surface. This iterative procedure is illustrated in [Figure 7](#). The original and refined constructions of the yield surface for config-0 are shown in [Figure 7\(b\)](#) and [\(d\)](#), respectively. Limited by the computing power and the high computational cost of DDD simulations, the data enrichment step cannot be continued beyond the first iteration, and we cannot obtain thousands of data points, a

typical number training data points for surface reconstruction (Williams et al., 2019). In this work, we perform one step of data enrichment and our final yield surface is trained on 189 data points from DDD simulations.

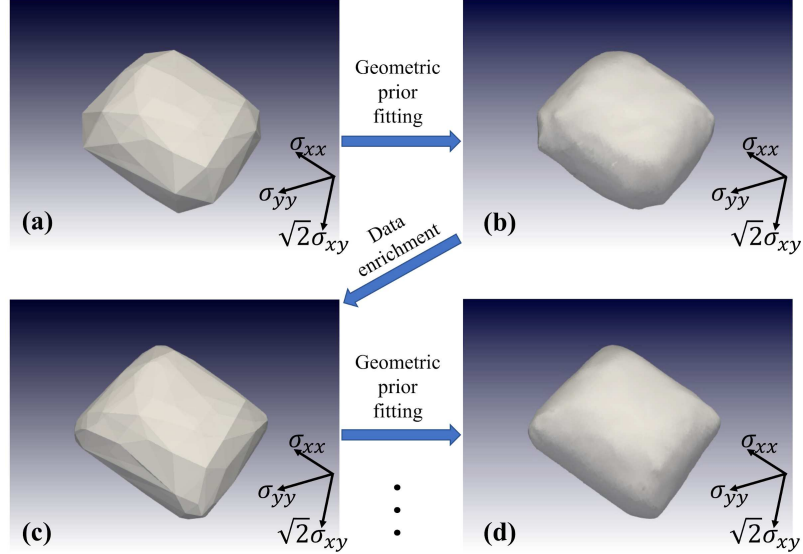


Figure 7: The geometric refinement of yield surface for config-0. (a) Yield surface is generated by interpolated triangulation from the initial 92 data points of yielding stress. (b) Based on (a), the yield surface is constructed by the fitting of geometric prior. (c) Based on (b), more sampling points are selected where DDD simulations are performed for data enrichment, resulting in 189 data points on the yield surface. (d) Based on (c) the yield surface is constructed by the fitting of geometric prior.

3. Results

3.1. Yield surfaces from plane stress loading

Figure 8 shows the yield surface constructed from the DDD simulations under plane stress loading from the initial dislocation configuration (config-0), together with how the yield surface evolves by plastic deformation along [100] and [110] directions, respectively. Figure 8 (a-c) show the yield surfaces from different viewing angles for config-0,

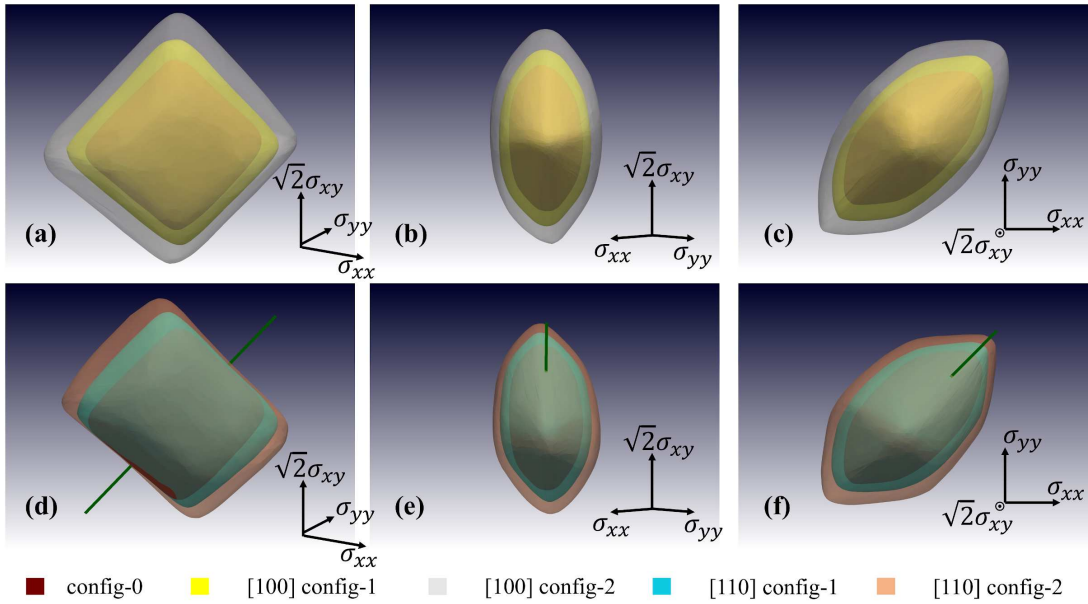


Figure 8: Along three different viewing angles, yield surfaces of (a-c) config-0, [100] config-1 and [100] config-2, and (d-f) config-0, [110] config-1 and [110] config-2 under plane stress loading. The green straight line in (d-f) denotes the stress orientation of uniaxial loading along [110] crystal orientation, i.e., $\hat{\sigma} = (1/2, 1/2, \sqrt{2}/2)$.

[100] config-1, [100] config-2. It can be seen that with increasing plastic strain along [100] crystal orientation, the yield surface appears to expand isotropically in all stress orientations. This indicates that plastic deformation along [100] direction results in *isotropic hardening*. Figure 8 (d-f) show the yield surfaces from different viewing angles for config-0, [110] config-1, [110] config-2. It can be seen that with increasing plastic strain along [110] crystal orientation, the expansion of the yield surface is not isotropic in all stress directions. Specifically, the yield surface appears to be not expanding appreciably along the stress orientations neighboring that of the [110] uniaxial loading itself. (The stress orientation corresponding to [110] uniaxial loading is indicated by the green straight lines.) This is consistent with the low strain-hardening rate in the stress-strain curve of [110] loading

shown in Figure 3(b). However, in stress orientations “perpendicular” to that of the [110] uniaxial loading in the space of $(\sigma_{xx}, \sigma_{yy}, \sqrt{2}\sigma_{xy})$, the expansion of yield surface (i.e. strain hardening) is significant. This indicates that plastic deformation along [110] direction results in *latent hardening*, representing the phenomenon that yield stress and hardening rate are higher in previously unactivated slip systems than in the previously activated primary slip systems (Edwards et al., 1953; Nakada and Keh, 1969; Kocks and Mecking, 2003). Latent hardening has been reported in the experiments of FCC single crystals where the initial loading orientations are single-slip orientations, which lie in the central region of the stereographic triangle (Kocks and Brown, 1966; Jackson and Basinski, 1967; Wessels and Jackson, 1969). In comparison, the [110] loading direction is at a corner of the stereographic triangle and activates multiple slip systems.

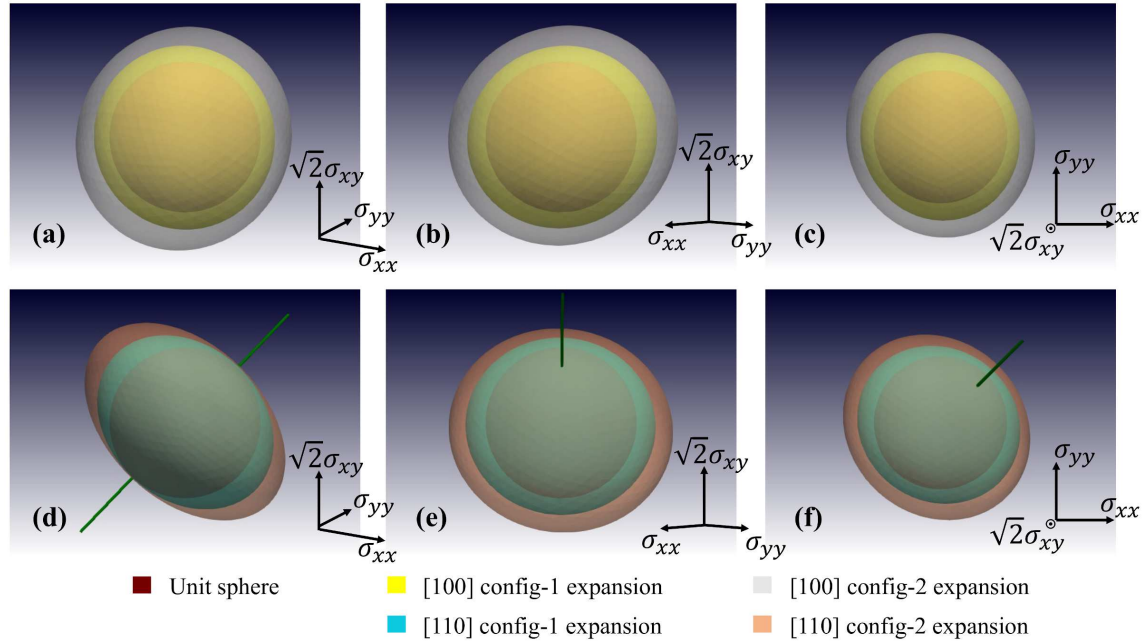


Figure 9: Hardening ratios of (a)-(c) [100] config-1 and [100] config-2, and (d)-(f) [110] config-1 and [110] config-2 in different perspectives. The innermost unit sphere is plotted as a reference. The stress orientation $\hat{\sigma} = (1/2, 1/2, \sqrt{2}/2)$ of the [110] uniaxial loading is shown as a green line.

To better illustrate the strain hardening behaviors, in [Figure 9](#) we plot the hardening ratio, which is defined as the yield surfaces at different plastic strains over the initial yield surface (i.e. config-0). (The innermost shape is a unit sphere plotted as a reference.) For each configuration, the orientation-dependent hardening ratio data is fitted to an ellipsoid for smoothing. [Figure 9](#) (a-c) shows that for plastic deformation along [100] crystal orientation, the hardening ratio is nearly isotropic in all stress orientations. In contrast, [Figure 9](#) (d-f) shows that for plastic deformation along [110] crystal orientation, the hardening ratio is close to 1 (i.e. no hardening) along the stress orientation corresponding to the [110] loading orientation itself, and is greater than 1 and nearly isotropic in the stress orientations perpendicular (in the $\hat{\sigma}$ space) to that of [110] uniaxial loading.

For a more detailed examination of how the yield surface evolves with plastic strain, [Figure 10](#) plots the cross-section views of the yield surfaces for different cut-planes in the space of stress orientations. When viewed on the cut-plane $(-\frac{\sqrt{2}}{2}, \frac{\sqrt{2}}{2}, 0)$, the yield surface for the original configuration (config-0) has approximately a square shape. [Figure 10\(a\)](#) shows that with [100] uniaxial loading, the cross-section view of the yield surface expands while keeping the square shape. In contrast, [Figure 10\(d\)](#) shows that with [110] uniaxial loading, the cross-section view of the yield surface expands asymmetrically into a rectangular shape. [Figure 10\(b-c\)](#) shows the cross-section views of yield surfaces under [100] uniaxial loading on cut-planes perpendicular to that in (a); the yield surface expands nearly isotropically in all directions. In comparison, [Figure 10\(e-f\)](#) shows corresponding views of yield surfaces under [110] uniaxial loading, where the expansion appears less in magnitude and is asymmetric.

3.2. Yield loci for uniaxial tension

Experimentally uniaxial loading tests are much easier to carry out than the general plane-stress loading (which may be performed on a tube with combined tension and torsion

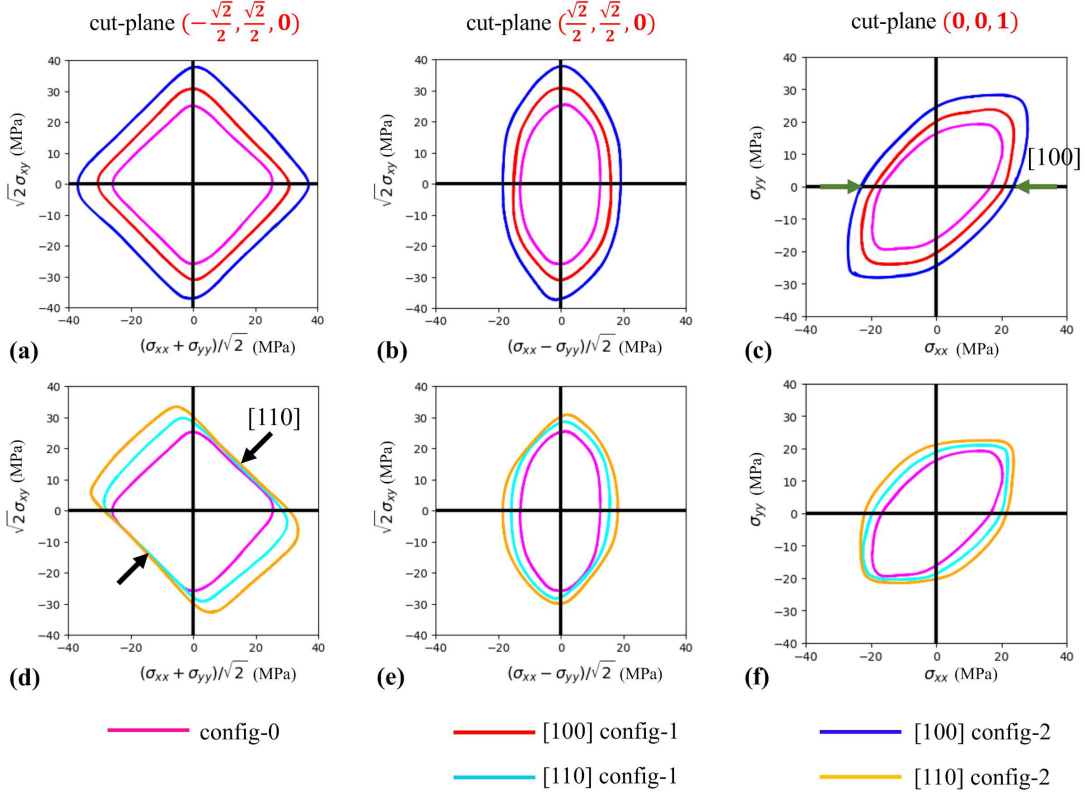


Figure 10: Cut-plane views of the yield surfaces of (a-c) config-0, [100] config-1 and [100] config-2, and (d-f) config-0, [110] config-1 and [110] config-2 under plane stress loading. The green and black arrows denote the stress orientations of [100] and [110] uniaxial loadings, respectively.

(Taylor and Quinney, 1931)). Therefore we examine the predicted yield conditions under uniaxial tension. The uniaxial tensile loading conditions correspond to a sub-set of stress orientations within the plane-stress conditions and are shown as the red circle on the unit sphere in Figure 2. Note that the center of the circle is not at the origin in the $\hat{\sigma}$ space. The central inversion of this circle with respect to the origin produces another circle, which corresponds to uniaxial compressive loading conditions.

Figure 11 plots the yield loci for the uniaxial tensile loading conditions, in terms of $\sqrt{2}\sigma_{xy}$ v.s. $(\sigma_{xx} - \sigma_{yy})/\sqrt{2}$. This figure corresponds to viewing the yield loci correspond-

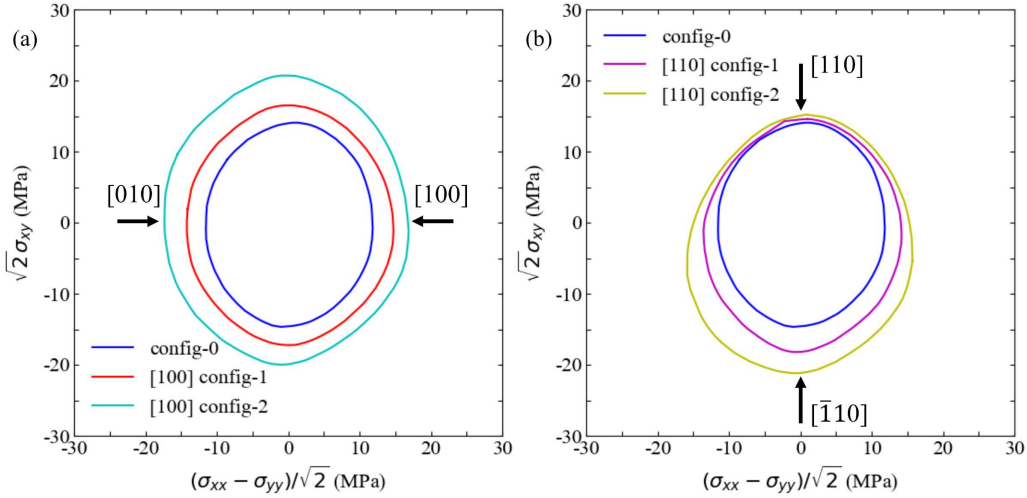


Figure 11: The 2D view of the yield loci along the $\hat{\sigma} = (\sqrt{2}/2, \sqrt{2}/2, 0)$ direction for uniaxial tensile loading applied to (a) config-0, [100] config-1 and [100] config-2, and (b) config-0, [110] config-1 and [110] config-2.

ing to uniaxial tension on the yield surface along the $\hat{\sigma} = (\sqrt{2}/2, \sqrt{2}/2, 0)$ direction. Figure 11(a) shows the evolution of yield loci from config-0 during plastic deformation along the [100] direction. The yield loci appears to expand isotropically while maintaining an oval shape. We note that the Von Mises (i.e. J_2) yield criterion (widely used for polycrystals) would predict the yield loci (for uniaxial tension) in the shape of a circle when plotted using these axes. Hence the deviation of the yield loci from a circle is a manifestation of the plastic anisotropy of single crystals. Figure 11(b) shows the evolution of yield loci from config-0 during plastic deformation along the [110] direction. There is little expansion of the yield loci around the [110] loading direction itself. But a substantial expansion is observed in the opposite end of the loop, corresponding to the $[\bar{1}10]$ loading orientation. The predictions of yield loci evolution from plastic deformation in the [110] loading direction, especially the pronounced latent hardening in the $[\bar{1}10]$ direction, provide new insight to the strain hardening behavior of FCC crystals. Existing experimental

studies on latent hardening in FCC crystals were usually conducted where the initial uniaxial loading is along a direction that favors single slip, i.e. only a single slip system is activated (Franciosi et al., 1980; Franciosi, 1985). Subsequently, a “daughter” sample is cut from the “parent” sample and then loaded in a different orientation. The goal was to let the primary slip system in the “daughter” sample interact strongly with the primary slip system previously activated in the “parent” sample, to cause latent hardening. We hope our prediction of the latent hardening behavior for initial loading along the [110] direction will motivate new experiments for its verification.

4. Discussion

4.1. Strain hardening mechanisms

The flow stress τ of a metal is known to correlate with the dislocation density ρ . In particular, the Taylor relation (Taylor, 1934), $\tau = \alpha\mu b \sqrt{\rho}$, is well supported by experimental data on polycrystals (Wang et al., 2021), where μ is the shear modulus, b is the Burgers vector magnitude, and α is a dimensionless constant. Here the total dislocation density for config-0 is $\sim 1.2 \times 10^{12} \text{ m}^{-2}$. After uniaxial deformation along [100] crystal orientation, the total dislocation density becomes $\sim 1.3 \times 10^{12} \text{ m}^{-2}$ and $\sim 2.0 \times 10^{12} \text{ m}^{-2}$, for config-1 and config-2, respectively. After uniaxial deformation along [110] crystal orientation, the total dislocation density becomes $\sim 1.3 \times 10^{12} \text{ m}^{-2}$ and $\sim 1.6 \times 10^{12} \text{ m}^{-2}$, for config-1 and config-2, respectively. Although in both deformation orientations, the strain hardening is accompanied by an increase of total dislocation density, this does not explain the difference between the isotropic hardening and latent hardening behaviors, for which an examination of dislocation density on individual slip systems is necessary.

Table 1 shows the dislocation densities on individual slip systems during uniaxial deformation along [100] direction. In FCC metals, there are 4 slip planes, each having 3

Table 1: Schmid factors and dislocation densities (in 10^{11} m^{-2}) for the 12 slip systems in various dislocation configurations (Config-0, Config-1 and Config-2) extracted from the [100] uniaxial loading. The active slip systems are highlighted in gray. Slip system index: i , Slip plane: **n**, Burgers vector: **b**, Schmid-Boas notation: **SB**, Schmid factors: **SF**

i	n	b	SB	SF	Config-0	Config-1	Config-2
1	($\bar{1}11$)	$\frac{1}{2}[0\bar{1}1]$	A2	0	0.6945	0.6354	1.0221
2	($\bar{1}11$)	$\frac{1}{2}[101]$	A3	0.4082	0.8599	0.8833	1.4480
3	($\bar{1}11$)	$\frac{1}{2}[110]$	A6	0.4082	0.8882	1.0106	1.7339
4	(111)	$\frac{1}{2}[0\bar{1}1]$	B2	0	0.7711	0.5372	1.0167
5	(111)	$\frac{1}{2}[\bar{1}01]$	B4	0.4082	0.6238	0.8580	1.3295
6	(111)	$\frac{1}{2}[\bar{1}10]$	B5	0.4082	0.8691	1.2066	1.9012
7	($\bar{1}\bar{1}1$)	$\frac{1}{2}[011]$	C1	0	0.8838	0.8195	1.0448
8	($\bar{1}\bar{1}1$)	$\frac{1}{2}[101]$	C3	0.4082	0.7518	0.8251	1.2895
9	($\bar{1}\bar{1}1$)	$\frac{1}{2}[\bar{1}10]$	C5	0.4082	0.8541	0.7792	1.1405
10	($1\bar{1}1$)	$\frac{1}{2}[011]$	D1	0	0.7214	0.5979	0.8278
11	($1\bar{1}1$)	$\frac{1}{2}[\bar{1}01]$	D4	0.4082	0.7460	0.7744	1.4479
12	($1\bar{1}1$)	$\frac{1}{2}[110]$	D6	0.4082	0.6779	0.6584	0.9163

slip directions, with a total of 12 slip systems. For uniaxial loading along [100] direction, 8 slip systems (2 on every slip plane) are activated with the same Schmid factor. (The remaining 4 slip systems have zero Schmid factor.) Table 1 shows that the dislocation densities on the active slip systems increase with strain for both config-1 (strained to 0.07%, except the slight decrease for C5 and D6 slip systems) and config-2 (strained to 0.22%). On the inactive slip systems (A2, B2, C1, D1), the dislocation densities in config-1 is actually lower than those in config-0; however, the dislocation densities on these slip systems in config-2 exceed those in config-0. This phenomenon is termed “slip-

free multiplication” (Akhondzadeh et al., 2021), because dislocations multiply on these slip systems with zero Schmid-factor and zero shear strain rate. Slip-free multiplication has been linked to coplanar interactions between active slip systems on the same slip plane (e.g. dislocations on inactive slip system A2 are produced because both A3 and A6 are active). We conclude that the isotropic hardening produced by plastic deformation along [100] is mainly because all 4 slip planes have 2 slip systems activated resulting in increased dislocation density on all slip planes. The slip-free multiplication is deemed not essential for the isotropy of strain hardening, because even though dislocation densities on inactive slip systems (A2, B2, C1, D1) are lower in config-1 than in config-0, the yield surface of config-1 appears to have expanded isotropically from that of config-0 nonetheless. In other words, having dislocations multiply on 2 out of 3 of slip systems on all 4 slip planes appears to be sufficient for isotropic hardening. Existing experiments also suggest that the difference of hardening behaviors in FCC single crystal metals depends on the activated slip planes instead of the slip directions or slip systems (Kocks and Brown, 1966).

[Table 2](#) shows the dislocation densities on individual slip systems during uniaxial deformation along [110] direction, in which only 4 slip systems (B2, B4, C1, C3) are activated with the same Schmid factor. The remaining 8 slip systems have zero Schmid factor. All slip systems on slip planes A and D are inactive. [Table 1](#) shows that the dislocation densities on the active slip systems increase with strain for both config-1 (strained to 0.07%) and config-2 (strained to 0.22%). On the inactive slip systems B5 and C5, the dislocation densities first decrease (in config-1) and eventually increase (in config-2), due to slip-free multiplication (because their coplanar slip systems B2, B4 and C1, C3 are active). On the other hand, all slip systems on slip planes A and D are inactive; consequently slip-free multiplication does not occur for these slip systems and their dislocation densities only decrease with strain. We conclude that the latent hardening produced by plastic deformation along [110] crystal orientation is due to the highly uneven dislocation

Table 2: Schmid factors and dislocation densities (in 10^{11} m^{-2}) for the 12 slip systems in various dislocation configurations (Config-0, Config-1 and Config-2) extracted from the [110] uniaxial loading. The active slip systems are highlighted in gray. Slip system index: i , Slip plane: **n**, Burgers vector: **b**, Schmid-Boas notation: **SB**, Schmid factors: **SF**

i	n	b	SB	SF	Config-0	Config-1	Config-2
1	($\bar{1}11$)	$\frac{1}{2}[0\bar{1}1]$	A2	0	0.6945	0.5536	0.4540
2	($\bar{1}11$)	$\frac{1}{2}[101]$	A3	0	0.8599	0.6544	0.5682
3	($\bar{1}11$)	$\frac{1}{2}[110]$	A6	0	0.8882	0.7212	0.5563
4	(111)	$\frac{1}{2}[0\bar{1}1]$	B2	0.4082	0.7711	1.0985	1.4954
5	(111)	$\frac{1}{2}[\bar{1}01]$	B4	0.4082	0.6238	1.0217	1.3904
6	(111)	$\frac{1}{2}[\bar{1}10]$	B5	0	0.8691	0.8092	1.1442
7	($\bar{1}\bar{1}1$)	$\frac{1}{2}[011]$	C1	0.4082	0.8838	1.5671	2.4345
8	($\bar{1}\bar{1}1$)	$\frac{1}{2}[101]$	C3	0.4082	0.7518	0.9866	1.6820
9	($\bar{1}\bar{1}1$)	$\frac{1}{2}[\bar{1}10]$	C5	0	0.8541	0.5988	0.9298
10	(1 $\bar{1}1$)	$\frac{1}{2}[011]$	D1	0	0.7214	0.5783	0.4366
11	(1 $\bar{1}1$)	$\frac{1}{2}[\bar{1}01]$	D4	0	0.7460	0.5217	0.3388
12	(1 $\bar{1}1$)	$\frac{1}{2}[110]$	D6	0	0.6779	0.5183	0.4730

densities on different slip planes. For example, if a sample first deformed along the [110] direction is unloaded and then reloaded along the [$\bar{1}10$] direction, then the slip systems A2, A3, D1, D4 will be activated; dislocations on these slip systems will interact strongly with existing ones on B2, B4, C1, C3 through glissile and collinear junctions (although no Lomer junctions).

4.2. Next steps in DDD simulations

In this work, we have demonstrated that DDD simulations can be used to construct the yield surface of single-crystal Cu under plane-stress conditions and how the yield sur-

face evolves under plastic deformation along uniaxial tensile deformation along [100] and [110] directions. Due to computational limits on the simulation time scale, the yield surface calculations are calculated under a stress rate of $10^{13} \text{ Pa} \cdot \text{s}^{-1}$, which is equivalent to the strain rate of 10^3 s^{-1} for the uniaxial deformation. However, what we usually have in mind when discussing yield surface or strain-hardening behaviors as well as most of the existing experimental data pertain to much lower, quasi-static strain rates, ranging from 10^{-4} s^{-1} to 10^{-1} s^{-1} (Meyers, 1994; Meyers and Chawla, 2008). Since strain-rate effect on the plastic deformation exists in most of the materials (Meyers, 1994), including polymers (Farrokh and Khan, 2010), metals (Butcher and Karnes, 1966; Meyers, 2012) and composites (Sierakowski, 1997), it is expected that the yield surface of single crystal copper is strain-rate dependent. At present, lowering the strain-rate of DDD simulations to the level of, say 10^{-3} s^{-1} , by brute force appears out of reach. Fortunately, existing experimental data (Edington, 1969) suggests that the flow stress of single-crystal Cu appears to be strain-rate independent in a wide range of strain-rates from 10^{-4} s^{-1} to 10^1 s^{-1} . DDD simulations of single-crystal Cu at the strain rate of 10^2 s^{-1} have been reported earlier (Sills et al., 2018). Hence DDD simulations at the strain rate of 10^1 s^{-1} appear feasible in the near future, with a bigger commitment of computational resources. A challenge that one may need to face is that the size of the DDD simulation cell is likely to increase in order to reach convergence when the strain-rate is lowered, which would further increase the computational cost.

In addition, more DDD simulations would be needed if we wish to go beyond the confines of plane-stress loading conditions and construct the yield surface in the general 6-dimensional stress space. It also appears necessary to repeat DDD simulations under the same stress conditions for different initial dislocation configurations to improve statistics.

4.3. Next steps in geometric prior method

We have demonstrated that the geometric prior method can be used to construct the yield surface as a manifold in stress space based on data obtained from DDD simulations. So far, the manifolds corresponding to each dislocation configuration (e.g. [100] config-1, [100] config-2, etc.) are constructed independently of each other, even though they are related to each other through plastic deformation starting from a common configuration (config-0). As a natural next step, it would be of interest for the geometric prior method to learn not only the yield surfaces separately, but its evolution with plastic deformation. Such a model is what is ultimately needed in a continuum constitutive model of crystal plasticity.

Intuitively, a starting point for modeling the evolution of the yield surface is to generate enough snapshots of the yield surface at different plastic deformation levels. However, the number of yield surfaces that can be obtained from DDD simulations is limited due to the high computational cost. Hence an interpolation scheme is needed between sparse data points along the strain axis. Based on differential manifold theory ([Kreyszig, 2013](#)), the interpolation between two yield surfaces should be rigorously defined by a transformation mapping from one manifold to another one. To derive an interpolation policy from a manifold transformation, it is necessary that the two underlined surfaces are isomorphic, i.e., it is required to establish the one-to-one correspondence between two points on these two surfaces. This appears to be a valid assumption at the strain level accessible to DDD simulations in the near future.

For the geometric prior method used in this study, we use a few patches to describe the local features of a yield surface. The patches can overlap and then provide a complete description of the entire yield surface. To achieve an accurate description of yield surface in this work, different numbers of patches are used for various yield surfaces and the patch number varies from 30 to 37. If two yield surfaces are represented by different number

of patches, it is difficult to build point-to-point mapping between them for interpolation. Therefore, in the next step, the yield surfaces from two configurations along the same deformation trajectory should be described by the same number of patches. One promising approach is to put effort to the parameterization of the motions of individual patches (translation, scaling, rotation, ...). This would allow us to construct a plasticity evolution law by establishing functional relationships between the patch motion parameters and the cumulative plastic strain ([Xiao and Sun, 2022](#)). Efforts are needed to maintain consistency between patches in the overlapping regions in this new scheme ([Xiao and Sun, 2022](#)).

To extend the yield surface to the full stress space (six-dimensional), one promising approach would be turning back to the implicit yield function representation but fitting it with neural kernel method ([Xiong et al., 2023](#)), so that the yield surface is constituted by a smooth basis extracted from kernel regression. This generally produce a smoothed yield surface with good generalizability, i.e., the yield surface will not deform to complex shapes locally due to insufficient training data, but some accuracy will be lost at locations with real geometric complexities. Essentially, in more-than-three-dimensional spaces, the hyper-surface reconstruction is still a challenging task, and the trade-off between local accuracy and global generalizability is more difficult to make than the cases in three-dimensional spaces.

5. Conclusions

In this work, we demonstrate a framework to construct the yield surface of single crystals using DDD simulations and the geometric prior method. DDD simulations under constant stress-rate conditions have been performed to identify the yielding conditions and the data are used by the geometric prior method to construct a cross-section of the yield surface as a manifold in the 3-dimensional sub-space of plane-stress. An iterative workflow is adopted, where the geometric prior method identifies regions of interest (based

on local curvature) where further sampling of the stress conditions by DDD simulations is performed.

We found that the yield surface evolves differently by plastic deformation along the [100] and [110] loading directions, respectively. Isotropic hardening is observed for [100] deformation, in which the yield surface expands with strain by nearly the same ratio in all stress orientations. This is traced to dislocation multiplication on all four slip planes during [100] deformation. In contrast, latent hardening is observed for [110] deformation, in which the yield surface does not expand much at all in the vicinity of the stress orientations corresponding to [110] tension, but expands significantly in other orientations. This is traced to dislocation multiplication on only two out of the four slip planes during [110] deformation.

6. Acknowledgements

This work was supported by the National Science Foundation, under Award Number DMREF 2118522 (W.J. and W.C.). W.C.S. and X.M. is supported by the UPS Foundation Visiting Professorship from Stanford University, with additional support from the National Science Foundation under grant contracts CMMI-1846875 and the Dynamic Materials and Interactions Program from the Air Force Office of Scientific Research under grant contracts FA9550-21-1-0391 and FA9550-21-1-0027.

Appendix A. Constant stress rate vs constant strain rate loading

The comparison between the stress-strain curves for uniaxial tensile loading with constant stress rate of 10^{13} Pa·s $^{-1}$ and constant strain rate of 10^3 s $^{-1}$ along the [100] orientation is shown in [Figure A.1](#).

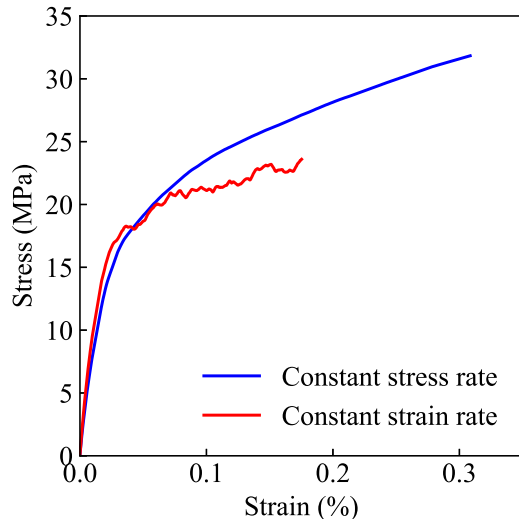


Figure A.1: The stress-strain curves for uniaxial tensile loadings with constant stress rate of 10^{13} Pa \cdot s $^{-1}$ and constant strain rate of 10^3 s $^{-1}$ along the [100] orientation, respectively.

Appendix B. DDD simulation parameters

The parameters of our DDD simulations are summarized in [Table B.1](#).

Table B.1: Summary of DDD simulation parameters for single crystal copper.

Property	Parameter	Value
Shear modulus	μ	54.6 GPa
Poisson's ratio	ν	0.324
Burgers vector magnitude	b	0.255 nm
Drag coefficient	B	$15.6 \mu \text{ Pa} \cdot \text{s}$
Core radius	a	$6 b$
Relative tolerance	f_{tol}	$0.1 b$
Absolute tolerance	r_{tol}	$10 b$
Threshold tolerance	r_{th}	$1 b$
Subcycling group 1 radius	r_{g1}	0
Subcycling group 2 radius	r_{g2}	$100 b$
Subcycling group 3 radius	r_{g3}	$600 b$
Subcycling group 4 radius	r_{g4}	$1600 b$
Max segment length	l_{max}	$2000 b$
Min segment length	l_{min}	$\sqrt{\frac{4}{\sqrt{3}} A_{\text{min}}}$
Max area between segments	A_{max}	$\frac{1}{2} \left(4A_{\text{min}} + \frac{\sqrt{3}}{4} l_{\text{max}}^2 \right)$
Min area between segments	A_{min}	$\min \left(2r_{\text{tol}} l_{\text{max}}, \frac{\sqrt{3}}{4} l_{\text{min}}^2 \right)$
Collision radius	r_{col}	$10 b$
Simulation cell size	L	$15 \mu\text{m}$
Strain rate for uniaxial loading	$\dot{\varepsilon}$	10^3 s^{-1}
Stress rate for plane stress loading	$\ \dot{\sigma}\ $	$10^{13} \text{ Pa} \cdot \text{s}^{-1}$

References

- Akhondzadeh, S., Bertin, N., Sills, R.B., Cai, W., 2021. Slip-free multiplication and complexity of dislocation networks in fcc metals. *Mater. Theory* 5, 1–24.
- Akhondzadeh, S., Sills, R.B., Bertin, N., Cai, W., 2020. Dislocation density-based plasticity model from massive discrete dislocation dynamics database. *J. Mech. Phys. Solids* 145, 104152.
- Amodeo, R.J., Ghoniem, N.M., 1990. Dislocation dynamics. i. a proposed methodology for deformation micromechanics. *Phys. Rev. B* 41, 6958.
- Arsenlis, A., Cai, W., Tang, M., Rhee, M., Oppelstrup, T., Hommes, G., Pierce, T.G., Bulatov, V.V., 2007. Enabling strain hardening simulations with dislocation dynamics. *Modelling Simul. Mater. Sci. Eng.* 15, 553.
- Bauschinger, J., 1886. On the change of the position of the elastic limit of iron and steel under cyclic variations of stress. *Mitt. Mech.-Tech. Lab.*, Munich 13.
- Berger, M.J., Oliger, J., 1984. Adaptive mesh refinement for hyperbolic partial differential equations. *J. Comput. Phys.* 53, 484–512.
- Bertin, N., Aubry, S., Arsenlis, A., Cai, W., 2019. Gpu-accelerated dislocation dynamics using subcycling time-integration. *Modelling Simul. Mater. Sci. Eng.* 27, 075014.
- Bowers, J., Wang, R., Wei, L.Y., Maletz, D., 2010. Parallel poisson disk sampling with spectrum analysis on surfaces. *ACM Trans. Graph. (TOG)* 29, 1–10.
- Butcher, B., Karnes, C., 1966. Strain-rate effects in metals. *J. Appl. Phys.* 37, 402–411.

- Coombs, W.M., Motlagh, Y.G., 2017. Nurbs plasticity: yield surface evolution and implicit stress integration for isotropic hardening. *Comput. Methods Appl. Mech. Eng.* 324, 204–220.
- Coombs, W.M., Motlagh, Y.G., 2018. Nurbs plasticity: non-associated plastic flow. *Comput. Methods Appl. Mech. Eng.* 336, 419–443.
- Coombs, W.M., Petit, O.A., Motlagh, Y.G., 2016. Nurbs plasticity: Yield surface representation and implicit stress integration for isotropic inelasticity. *Comput. Methods Appl. Mech. Eng.* 304, 342–358.
- Cuturi, M., 2013. Sinkhorn distances: Lightspeed computation of optimal transport. *Adv. Neural Inf. Process.* 26.
- Dahl, V.A., 2023. Icosphere 0.1.3. <https://pypi.org/project/icosphere/>.
- Devincre, B., Kubin, L.P., 1997. Mesoscopic simulations of dislocations and plasticity. *Mater. Sci. Eng. A* 234, 8–14.
- Edington, J., 1969. The influence of strain rate on the mechanical properties and dislocation substructure in deformed copper single crystals. *Philos. Mag.* 19, 1189–1206.
- Edwards, E., PARKER, E., WASHBURN, J., 1953. Some observations on the work hardening of metals. *Trans. Metall. Soc. AIME* 197, 1525–1529.
- Farrokh, B., Khan, A.S., 2010. A strain rate dependent yield criterion for isotropic polymers: low to high rates of loading. *Eur. J. Mech. A/Solids* 29, 274–282.
- Franciosi, P., 1985. The concepts of latent hardening and strain hardening in metallic single crystals. *Acta Metall.* 33, 1601–1612.

- Franciosi, P., Berveiller, M., Zaoui, A., 1980. Latent hardening in copper and aluminium single crystals. *Acta Metall.* 28, 273–283.
- Hill, R., 1998. The mathematical theory of plasticity. volume 11. Oxford university press.
- Hirsch, P., Horne, R., Whelan, M., 1956. LXVIII. Direct observations of the arrangement and motion of dislocations in aluminium. *Philos. Mag.* 1, 677–684.
- Hirth, J., Lothe, J., 1982. Theory of Dislocations. Wiley.
- Jackson, P., Basinski, Z., 1967. Latent hardening and the flow stress in copper single crystals. *Can. J. Phys.* 45, 707–735.
- Kocks, U., Brown, T., 1966. Latent hardening in aluminum. *Acta Metall.* 14, 87–98.
- Kocks, U., Mecking, H., 2003. Physics and phenomenology of strain hardening: the fcc case. *Prog. Mater. Sci.* 48, 171–273.
- Kreyszig, E., 2013. Differential geometry. Courier Corporation.
- Meyers, M., 2012. Shock waves and high-strain-rate phenomena in metals: concepts and applications. Springer Science & Business Media.
- Meyers, M.A., 1994. Dynamic behavior of materials. John wiley & sons.
- Meyers, M.A., Chawla, K.K., 2008. Mechanical behavior of materials. Cambridge university press.
- Murtagh, F., 1991. Multilayer perceptrons for classification and regression. *Neurocomputing* 2, 183–197.
- Nakada, Y., Keh, A., 1969. Latent hardening in rock-salt type crystals. *Phys. Status Solidi B* 32, 715–730.

- Orowan, E., 1934. Plasticity of crystals. *Zeit. Fur Phys.* 89, 605–659.
- ParaDiS, 2023. Parallel dislocation simulator. <https://gitlab.com/opendis/ParaDiS-2.7>.
- Polanyi, M., 1934. Lattice distortion which originates plastic flow. *Zeit. Fur Phys.* 89, 660–662.
- Rubner, Y., Guibas, L.J., Tomasi, C., 1997. The earth movers distance, multi-dimensional scaling, and color-based image retrieval, in: Proceedings of the ARPA image understanding workshop, p. 668.
- Sierakowski, R.L., 1997. Strain rate effects in composites. *Appl. Mech. Rev.* 50, 741–761.
- Sills, R.B., Aghaei, A., Cai, W., 2016. Advanced time integration algorithms for dislocation dynamics simulations of work hardening. *Modelling Simul. Mater. Sci. Eng.* 24, 045019.
- Sills, R.B., Bertin, N., Aghaei, A., Cai, W., 2018. Dislocation networks and the microstructural origin of strain hardening. *Phys. Rev. Lett.* 121, 085501.
- Tang, W., Lin, Z., Gong, Y., 2023. Gc-net: An unsupervised network for gaussian curvature optimization on images. *J. Signal Process. Syst.* 95, 77–88.
- Tang, Y., Feng, J., 2018. Multi-scale surface reconstruction based on a curvature-adaptive signed distance field. *Comput. Graph.* 70, 28–38.
- Taylor, G.I., 1934. The mechanism of plastic deformation of crystals. part I.theoretical. *Proc. R. Soc. Lond. A* 145, 362–387.
- Taylor, G.I., Quinney, H., 1931. The plastic distortion of metals. *Phil. Trans. Roy. Soc. A* 230, 323–362.

- Vlassis, N.N., Sun, W., 2021. Sobolev training of thermodynamic-informed neural networks for interpretable elasto-plasticity models with level set hardening. *Comput. Methods Appl. Mech. Eng.* 377, 113695.
- Vlassis, N.N., Sun, W., 2022. Component-based machine learning paradigm for discovering rate-dependent and pressure-sensitive level-set plasticity models. *J. Appl. Mech.* 89.
- Wang, L., Lu, Z., Li, H., Zheng, Z., Zhu, G., Park, J.S., Zeng, X., Bieler, T.R., 2021. Evaluating the taylor hardening model in polycrystalline ti using high energy x-ray diffraction microscopy. *Scr. Mater.* 195, 113743.
- Wessels, E., Jackson, P., 1969. Latent hardening in copper-aluminium alloys. *Acta Metall.* 17, 241–248.
- Williams, F., 2022. Point cloud utils. <https://www.github.com/fwilliams/point-cloud-utils>.
- Williams, F., Schneider, T., Silva, C., Zorin, D., Bruna, J., Panozzo, D., 2019. Deep geometric prior for surface reconstruction, in: Proceedings of the IEEE/CVF Conference on Computer Vision and Pattern Recognition, pp. 10130–10139.
- Xiao, M., Sun, W., 2022. Geometric prior of multi-resolution yielding manifolds and the local closest point projection for nearly non-smooth plasticity. *Comput. Methods Appl. Mech. Eng.* 400, 115469.
- Xiong, Z., Xiao, M., Vlassis, N., Sun, W., 2023. A neural kernel method for capturing multiscale high-dimensional micromorphic plasticity of materials with internal structures. *Comput. Methods Appl. Mech. Eng.* 416, 116317.